Energy & Environmental Science

RSC Publishing

PAPER

View Article Online
View Journal | View Issue



Cite this: *Energy Environ. Sci.*, 2013, **6**, 963

# Kinetics and mechanism of solar-thermochemical $H_2$ production by oxidation of a cobalt ferrite–zirconia composite†

Jonathan R. Scheffe,‡[a] Anthony H. McDaniel,*[b] Mark D. Allendorf[b] and Alan W. Weimer[a]

Accurate knowledge of water splitting kinetics is essential for the design and optimization of high-temperature thermochemical cycles for solar-driven fuel production, but such crucial data are unavailable for virtually all redox materials of potential practical value. We describe an investigation of the redox activity and oxidation kinetics of cobalt ferrite, a promising material for this application that is representative of a broader class of metal-substituted ferrites. To enable repetitive cycling, ferrites must be supported on another oxide to avoid sintering and deactivation. Consequently, we synthesized a composite material using atomic layer deposition of cobalt and iron oxides on zirconia, a commonly used ferrite "support", to create a well-controlled, uniformly distributed composition. Our results show that the support is not an innocent bystander and that dissolved iron within it reacts by a different mechanism than embedded iron oxide particles in the matrix. Samples were thermally reduced at 1450 °C under helium and oxidized with steam at realistic process temperatures ranging from 900 °C to 1400 °C. Experiments within a fluid-dynamically well-behaved stagnation-flow reactor, coupled with detailed numerical modelling of the transient $H_2$ production rates, allow us to effectively deconvolve experimental artefacts from intrinsic material behaviour over the entire time domain of the oxidation reaction. We find that second-order reaction and diffusion-limited mechanisms occur simultaneously at different oxidation rates and involve iron in two separate phases: (1) reduced Fe dissolved in the $ZrO_2$ support and (2) iron oxide located at the interface between embedded ferrite particles and the zirconia matrix. Surprisingly, we also identified a catalytic mechanism occurring at the highest temperatures by which steady-state production of $H_2$ and $O_2$ occurs. The results reported here, which include Arrhenius rate constants for both oxidation mechanisms, will enable high-fidelity computational simulation of this complex, but promising approach to renewable fuel production.

Received 25th May 2012
Accepted 11th January 2013

DOI: 10.1039/c3ee23568h

www.rsc.org/ees

**Broader context**

Exploiting an otherwise underutilized global resource such as solar energy is critical to realizing environmentally sound and sustainable energy practices. However, the efficient collection and storage of solar energy continues to be an engineering challenge. One attractive alternative to photovoltaic- or photo-electrochemical-based approaches is concentrated solar power (CSP). Here, solar radiation in the form of process heat can be used to drive endothermic water-splitting reactions, thereby storing solar energy in a $H_2$ chemical bond. Successful development of CSP technologies for fuel synthesis, using non-volatile metal oxides as the working fluid in a two-step thermochemical cycle, relies upon knowing the solid-state processes underpinning the hydrogen evolution reaction in thermally reduced complex oxides. Often times these reactive materials are composites, which further complicates our understanding of the high-temperature oxidation chemistry. This article provides mechanistic insight into the solid-state behavior that governs hydrogen evolution as well as proposes a general framework upon which artifacts intrinsic to flow reactors can be removed so that the true kinetic behaviour is revealed.

## Introduction

Metal-substituted ferrites having the spinel structure and the general stoichiometry $M_xFe_{3-x}O_4$, where M represents Ni,[1,2] Zn,[3] Co,[4] or other transition metals, are promising materials for splitting water by the solar-driven, two-step redox cycle shown below:[5]

$$(M_xFe_{1-x})_3O_4 \xrightarrow{+\Delta} 3(M_xFe_{1-x})O + 0.5O_2 \quad (1)$$

[a]*Department of Chemical and Biological Engineering, 3415 Colorado Avenue, JSCBB Campus Box 596, Boulder, Colorado 80309-0424, USA*

[b]*Sandia National Laboratories, Livermore, California 94551-0969, USA. E-mail: amcdani@sandia.gov; Fax: +1 925-294-2276; Tel: +1 925-294-1440*

† Electronic supplementary information (ESI) available. See DOI: 10.1039/c3ee23568h

‡ Department of Mechanical and Process Engineering, ETH Zurich, 8092 Zurich, Switzerland.

$$3(M_xFe_{1-x})O + H_2O \xrightarrow{-\Delta} (M_xFe_{1-x})_3O_4 + H_2 \quad (2)$$

In this process, the first step is endothermic and occurs at a temperature above the second step, with heat provided by solar energy to reduce iron in the ferrite from $Fe^{3+}$ to $Fe^{2+}$. This typically occurs at temperatures greater than 1400 °C. In the second, lower-temperature reaction, the reduced oxide is exposed to steam to reoxidize it to the ferrite and produce $H_2$. The reduced product is either a solid solution with the wustite crystal structure, or a molten slag containing iron in both the 2+ and 3+ oxidation states as well as the $M^{2+}$ metal ion.[1] There are now numerous examples demonstrating this concept in a variety of reactor types.[6–9]

The kinetics and mechanism of ferrite thermochemical cycles, which are expected to play a critical role in both reactor design and overall process efficiency, are poorly understood, although other aspects of this chemistry have been examined in some detail. For example, the effects of metal substitution on ferrite reactivity have received considerable attention. The influence of $M_xFe_{3-x}O_4$ stoichiometry,[1,2,4] synthetic method,[4,10,11] and support material[2,12] on the total amount of $H_2$ produced, as well as the ability to be cycled have been characterized. Thermodynamic analysis of Fe, Co, Ni, and Zn substitution in $M_xFe_{3-x}O_4$, indicates that $x$ and the identity of M strongly influence the stability of the ferrite with respect to reaction (1) and, consequently, the amount of $H_2$ that can be produced for a given reduction temperature.[1] Although one investigation reported that $H_2$ yield from cobalt ferrite peaked at the non-stoichiometric composition $Co_{0.7}Fe_{2.3}O_4$,[4] subsequent investigations indicate that yield peaks at the stoichiometric composition (*i.e.*, $MFe_2O_4$)[1,2] in agreement with the thermodynamic analysis.[1] In general, this body of work shows that Co and Ni substitution significantly increases the extent of reduction at a given temperature relative to $Fe_3O_4$, which does not fully reduce until temperatures in excess of the melting point of wustite.

In contrast, the kinetics and mechanism of ferrite thermochemical cycles have received almost no attention. Charvin *et al.* studied the oxidation of FeO in the presence of steam and observed a strong dependence of $H_2$ production rate on FeO particle size during water oxidation experiments.[13] As the particle size was increased, slower rates were observed. This was attributed to formation of an oxide layer on the surface of the particles, hindering further oxidation of the bulk. Similar behaviour is observed for $CO_2$ reduction to carbon on chemically reduced $CoFe_2O_4$ nanoparticles.[14] In this case, early stages in the reduction of $CO_2$ appeared to be limited by reactions at the interfaces between nanoparticles in the compacted sample, while at later stages the reaction became limited by solid-state diffusion. Go *et al.* studied water oxidation by Mn and Zn substituted ferrite powders that were chemically reduced, concluding that the reaction is diffusion limited.[15] Neises *et al.* also investigated water oxidation by Zn ferrite, using a SiC honeycomb support. They determined that the kinetics agreed well with a shrinking core model; however, they also observed a significant interaction between the SiC support phase and active ferrite layer which was not accounted for in their kinetic analysis.[3] Finally, Loutzenhiser *et al.* monitored the oxidation of FeO particles by $CO_2$ as a function of temperature and oxidant partial pressure. They reported that the reaction is initially limited by surface chemistry, followed by a regime controlled by the diffusion of ions through the material,[16] which they simulated using a shell–core model similar to Neises *et al.*

An additional factor not addressed thus far is the impact of a support material such as YSZ or $ZrO_2$, even though its use is often essential for repeated cycling in a realistic solar application.[2,17] The use of support materials was originally introduced to stabilize the ferrite against sintering and consequent loss of reactivity due to the reduction in surface area. For example, Kodama *et al.* observed that both $H_2$ production and reproducibility over multiple reaction cycles improved when Ni, Co, and Fe ferrites were mixed with $ZrO_2$ and yttria-stabilized zirconia (YSZ) supports.[2,4,17] In addition, they determined that $Fe^{2+}$ forms a solid solution with these supports during thermal reduction. This dissolved iron appears to be more active or accessible than the ferrite, probably due to the high oxygen-ion transport rate through zirconia.

Here, we describe a detailed investigation of the water-splitting (WS) kinetics of thermally reduced cobalt ferrite supported on zirconia. Although the prior work discussed above provides a useful basis for understanding gas splitting by ferrites, actual kinetic data were reported only for materials that are unlikely to be practical. In particular, magnetite ($Fe_3O_4$) does not undergo deep reduction until temperatures exceeding the melting point of the FeO product are reached, while $ZnFe_2O_4$ decomposition yields volatile Zn-containing products that rapidly deplete the ferrite of that metal.[1] Cobalt- and nickel-substituted ferrites are more attractive for solar-driven water splitting, as their reduced-oxide product melts at higher temperatures than FeO and is much less volatile than zinc. We prepared a cobalt ferrite/*m*-$ZrO_2$ composite (20 mass% $Co_{0.9}Fe_{2.1}O_4$ in *m*-$ZrO_2$) using an atomic layer deposition (ALD) method we reported previously.[18] This approach allows uniform deposition onto high surface-area supports with pore sizes inaccessible to liquid-phase deposition methods, as well as facile control of the oxide composition and loading. The ALD material was sintered to create a dense composite that provides a reasonably well-controlled platform for measuring the WS kinetics and employing solid-state kinetic models to identify specific reaction regimes. In addition, we describe a previously unreported and surprising catalytic phenomenon at high temperatures, in which heterogeneous WS occurs to produce both $H_2$ and $O_2$. The results delineate limitations on the use of cobalt ferrites in solar-driven WS thermochemical cycles, as well as provide insight with respect to the design of novel materials having enhanced performance.

## Experimental methods

All materials were synthesized *via* sequential deposition of CoO and $Fe_2O_3$ films onto porous $ZrO_2$ supports (Alfa Aesar, S.A. 90 $m^2\ g^{-1}$ and median pore diameter of 400 Å) *via* atomic layer

 

deposition. Before synthesis, the supports were ground with a mortar and pestle and sieved below a 325 mesh. A detailed description of the synthesis procedure is documented in Scheffe *et al.*[18] The resulting material consisted of 20 mass% active ferrite material with a layer thickness of ~2 nm that was heat treated at 1450 °C in air for two hours, resulting in a dense, sintered powder. A JEOL 7600F field-emission scanning electron microscope (FESEM) operating at 4 kV and 15 kV was used to examine the microstructure and local chemical composition for both as-prepared ALD and post heat-treatment materials. SEM samples were mounted on conductive tape and sputtered with carbon. Elemental composition was determined *via* energy dispersive X-ray spectroscopy (EDS).

Following heat treatment the sintered samples were reduced and oxidized in a stagnation flow reactor (SFR), which has also been described elsewhere.[18] Salient features of the experimental apparatus consist of a stainless-steel gas-handling manifold, ceramic reactor core, high-temperature furnace, and modulated effusive-beam mass spectrometer. In stagnation flow, the gas-phase region above the sample between centre line and reactor wall can be considered an ideal one-dimensional stagnation plane governed by diffusive transport. This is an important attribute that distinguishes the fluid dynamics of this reactor type from others typically used to characterize kinetic behaviour of ferrites and other materials used in thermochemical cycles, namely, packed bed reactors,[19] flow tube reactors,[3] and flow geometries common to thermogravimetric analysers (TGA).[16] It is also important to note that in the SFR, sample material is placed in a loosely packed shallow bed where gases have access to all exposed surfaces and are well mixed within the control volume at the temperatures and pressures used in this experiment.

Mass flow controllers were used to meter all gas feed rates. The reactor exhaust was throttled, allowing for feedback control of the reactor pressure to any desired set point within the range 1–760 Torr. Water was delivered through an evaporator fed by a micro-syringe pump. Between 50 and 200 mg of sample were placed in the reactor. Thermal reduction (TR) was accomplished by heating the sample to 1450 °C in a helium flow (500 sccm) for 100 minutes. WS was performed using 20–40 vol% steam in He with a total flow rate of 500 sccm over a 1000 s time interval. WS temperatures ranged from 900 °C to 1400 °C. A single sample was used over the course of the experimental campaign and sequentially cycled more than 15 times. The total reactor pressure for both TR and WS was 75 Torr.

Gases exiting the flow reactor were sampled using a differentially pumped, modulated effusive beam mass spectrometer (Extrell C50, 500 amu). Molecular oxygen ($m/z = 32$) was monitored during TR and molecular hydrogen ($m/z = 2$) during WS at a data collection rate of approximately 1.8 Hz. A liquid nitrogen-filled cryogenic trap was used to condense water before gases were sampled by the mass spectrometer. In post-measurement data analysis, a numerical procedure was used to remove the effects of detector time lag and dispersion/mixing downstream of the reactor on the observed rates of gas production. Analytical standards for $O_2$ and $H_2$ were used to calibrate the mass spectrometer.

## Computational methods

The evolution of $H_2$ during the WS reaction is an inherently transient response governed by non-equilibrated surface and bulk-mediated processes that commence upon exposure to water vapour. Characteristic temporal behaviour of the $H_2$ production rate measured during WS is illustrated in the left panel of Fig. 1, which shows a sharp increase in $H_2$ that peaks at relatively short times, followed by a gradual decline. The observed behaviour is certainly a reflection of the rate-governing mechanisms in the material, namely surface reactions and bulk diffusion of reactive intermediates. However, physical processes intrinsic to the experimental apparatus, such as detector time lag and gas-phase dispersion, complicate interpretation of the temporal response. Consequently, it is necessary to apply a more comprehensive analytical treatment to the data to separate these experimental affects and reveal the true nature of the material behaviour.

A numerical approach to analysing the transient $H_2$ production rates observed during WS was devised that accounts for: (1) kinetic processes occurring in the solid state; (2) the finite time required to introduce water vapour into the reacting volume; (3) detector time lag; and (4) dispersion/mixing of the $H_2$ evolved from the solid surface as it is transported downstream of the reactor volume to the detector. Impacts of the aforementioned experimental artefacts (namely 2–4 listed above) were not fully addressed by previous researchers even though they can lead to erroneous conclusions regarding both the nature of rate limiting processes and the energetics associated with them (see Fig. S3 and S4 in the ESI†).

Here, the concepts of solid-state kinetic theory[20,21] were used without modification to describe the chemical and physical changes occurring in the material. A transient, three-dimensional simulation of the inlet gas-handling manifold and ceramic body were used to establish a lower-order functional

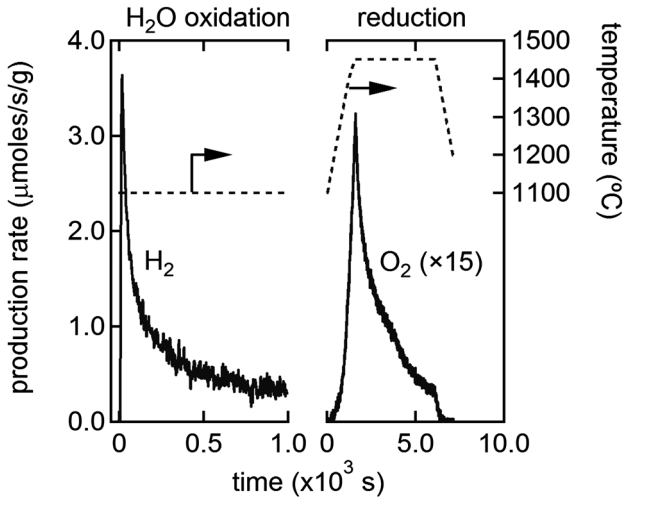


**Fig. 1** $H_2$ production rate measured during oxidation at 1100 °C and 30 vol% $H_2O$ (left), and the subsequent rate of evolved $O_2$ measured during thermal reduction at 1450 °C (right). The rates are normalized to the mass of ferrite in the sample.

form for the time-dependent flow rate of water vapour into the reactor volume. A continuously stirred tank reactor (CSTR) model was used to approximate flow effects downstream of the reactor volume. Finally, kinetic parameters for the solid-state reactions were extracted from experimental observations by minimizing a weighted, least-squares objective function that compares predicted values to measurements at every time step.

The system of equations used to simulate the experimental data and determine the residual sum of squares error (RSSQ) is as follows:

$$\frac{d\alpha_{i,k}}{dt} = A_i e^{\left[-\frac{E_i}{RT}\right]}\left[Y_{H_2O,0,k}(t - t_{s,k})\right]^{\gamma_{H_2O,i}} f(\alpha_i) \quad (3)$$

$$\frac{d\alpha_{tot,k}}{dt} = \sum_i \frac{d\alpha_{i,k}}{dt}; \quad \alpha_{tot,k} \leq 1 \quad (4)$$

$$\frac{dY_{H_2,n,k}}{dt} = \tau_k\left(Y_{H_2,n-1,k} - Y_{H_2,n,k}\right) \quad (5)$$

$$Y_{H_2,0,k} = \frac{V_{H_2,k}}{F_{tot,k}}\frac{d\alpha_{tot,k}}{dt} \quad (6)$$

$$RSSQ = \sum_k \sum_t \omega_{H_2,k}\left[\overline{Y}_{H_2,k} - Y_{H_2,n=last,k}\right]^2 \quad (7)$$

Definitions for notation can be found in Table 1 and a schematic that illustrates the modelling approach is presented in Fig. S1.† Eqn (3) represents the extent of reaction as predicted by solid-state kinetic theory.[20,21] Functional forms for $f(\alpha_i)$were taken directly from a pallet of 14 validated mathematical expressions for various rate-limiting mechanisms applicable to the phenomena under investigation. A subset of this pallet can also be found in Table 1, which shows the expressions that result in best fits to the data. Eqn (4) balances the global reaction extent when two or more competing mechanisms are evaluated. Eqn (5) is a series CSTR model and eqn (6) is the proportionality relationship between $H_2$ mole fraction and reaction extent.

The number of CSTRs in series ($n$) was either 2 or 3, depending on the experimental conditions used. In particular, this number depends on the amount of water vapour in the flow stream and was determined by conducting separate $H_2$ and CO tracer experiments in the SFR (Fig. S2†). The number of oxidation experiments or runs ($k$) was 12 and the number of solid-state processes occurring simultaneously ($i$) was either 1 or 2. The inlet mole fraction for water vapour ($Y_{H_2O,0,k}$) was based on a time-shifted error function that produced an appropriately shaped sigmoidal curve (Fig. S1†). It should also be noted that when an order-based model (F2 in Table 1) is paired with a diffusion or shrinking core model, the water concentration dependence term is only applied to the order-based equation.

Conceptually, the system of ordinary differential equations (eqn (3)–(5)) describes a transient process in which $H_2$ is produced by one or two solid-state mechanisms occurring irreversibly within a perfectly mixed control volume containing the active material. This product gas is then transported through a series of CSTRs that alters the temporal characteristics of the $H_2$ signal. There are at most eight unknowns in this system, the triplet ($A_i$,$E_i$,$\gamma_{H_2O,i}$; $i = 1,2$) and the choice for kinetic model ($f(\alpha_i)$; $i = 1,2$), which are resolved by fitting to experimental data. The computational tool Mathematica®[22] was used to numerically solve the system of governing equations (NDSolve), produce a value for the RSSQ shown in eqn (7), and then pass this information to a numerical minimization routine (NMinimize). The fitting routine uses a Differential Evolution algorithm native to Mathematica® that stochastically solves a constrained, mixed-integer optimization problem (kinetic parameters $\in \mathbb{R}$, and model choice $\in \mathbb{N}$). Constraints take the form of inequalities and brick-wall penalty functions. Differential weighting is also applied to data points surrounding the peak in $H_2$ signal ($10 < t < 400$ s), and to a lesser extent, the tails observed at $t > 400$ s.

## Results

### Thermal reduction and water oxidation reactions

The redox-active cobalt ferrite spinel was deposited as described above on substrate particles *via* ALD, resulting in homogeneous thin films of $Co_{0.9}Fe_{2.1}O_4$.[18] An SEM image of the as-deposited material is shown in panel (a) of Fig. 2, where primary particles

**Table 1** Model nomenclature and definitions for $f(\alpha_i)$

| Symbol | Description | Units |
|---|---|---|
| $\alpha_{i,k}$ | Extent of reaction for the $i^{th}$ process and $k^{th}$ run | None |
| $\alpha_{tot,k}$ | Total extent of reaction for $k^{th}$ run | None |
| $A_i$ | Pre-exponential factor for the $i^{th}$ process | 1/s |
| $E_i$ | Activation energy for the $i^{th}$ process | J mol$^{-1}$ |
| $\gamma_{j,i}$ | Reaction order for $j^{th}$ species in the $i^{th}$ process | None |
| $Y_{j,n,k}$ | Mole fraction of $j^{th}$ species in the $n^{th}$ reactor and $k^{th}$ run | None |
| $\tau_k$ | Space velocity for $k^{th}$ run | 1/s |
| $t_{s,k}$ | Detector lag time for the $k^{th}$ run | s |
| $V_{j,k}$ | Standard volume of $j^{th}$ species in $k^{th}$ run | scm$^3$ |
| $F_{tot,k}$ | Standard total flow rate for $k^{th}$ run | scm$^3$ s$^{-1}$ |
| $\omega_{j,k}$ | Weighting factor for $j^{th}$ species in $k^{th}$ run | None |
| F2 | $f(\alpha_i) = (1 - \alpha_i)^2$, second order reaction | |
| D1 | $f(\alpha_i) = 1/(2\alpha_i)$, 1-D diffusion | |

 

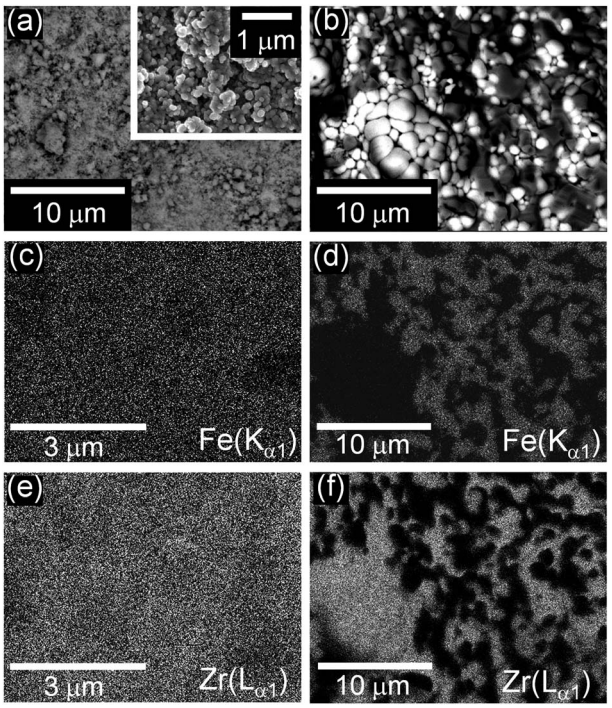


**Fig. 2** SEM micrographs of 20 mass% $Co_{0.9}Fe_{2.1}O_4$ deposited on *m*-$ZrO_2$ before heat treatment (a) and after (b). EDS maps of the Fe($K_{\alpha1}$) absorption edge (light areas) before heat treatment (c) and after (d). EDS maps of the Zr($L_{\alpha1}$) absorption edge (light areas) before heat treatment (e) and after (f).

with diameters in the range of 100–200 nm are easily visible, indicating that little or no sintering occurs during the ALD process. Additionally, X-ray fluorescence maps of Fe($K_{\alpha1}$) and Zr($L_{\alpha1}$) absorption edges, shown in panels (c) and (e) in Fig. 2, indicate that a homogeneous dispersion of these elements is achieved. Following heat treatment at 1450 °C in air (a realistic temperature for TR), the substrate particles become noticeably sintered and Zr and Fe/Co phases segregate, as evidenced by SEM images and EDS elemental maps (panels b, d, and f in Fig. 2). The resulting microstructure is similar to ferrite/$ZrO_2$ composites that have been used in high temperature thermochemical cycles and described elsewhere in the literature.[2,4,17] Here, primary particles of order 1 μm in diameter are clearly evident among a high density of grain boundaries and distinct regions containing high concentrations of either Zr or Fe are revealed by EDS.

The sintered cobalt ferrite/$ZrO_2$ composite material was thermally reduced at 1450 °C in helium and subsequently re-oxidized by exposure to various concentrations of water vapour. Representative production rates normalized to the ferrite mass for $H_2$ (measured at 1100 °C oxidation temperature and 30 vol% $H_2O$) and $O_2$ are presented in Fig. 1. These data show that, despite having been sintered, the redox activity of the ferrite is preserved. Oxidation *via* WS is much more rapid than TR and occurs primarily within the first 1000 s of water vapour exposure. As mentioned previously, the WS reaction is characterized by a sharp peak in the $H_2$ production rate at early times followed by a gradual decay, which is behaviour characteristic of other ferrite/composite WS chemistry reported in the literature.[3,12] Note that the $H_2$ production rate plateaus at times longer than 900 s. The magnitude of this plateau above baseline is even greater at oxidation temperatures in excess of 1200 °C and does not return to baseline even after long periods of water vapour exposure. The time required for TR is much longer than WS and after 6000 s oxygen evolution is still not complete. A near-stoichiometric ratio of $H_2/O_2$ is observed under all WS conditions below an oxidation temperature of 1200 °C.

We observe that the total amount of $H_2$ produced during WS is highly dependent upon the oxidation temperature; the total amount of $O_2$ produced during TR subsequent to WS is also temperature dependent. These observations are summarized in Fig. 3, where the total $O_2$ *versus* total $H_2$ is plotted along with the ideal 1 : 2 stoichiometric trend line. The WS temperature increases from left to right. Because WS thermodynamics are more favourable at lower temperatures,[1] we attribute this trend to the kinetics of the reaction; the measured yields are limited by the amount of time the sample experiences oxidative conditions (1000 s in this case). Cobalt ferrite samples were also compared to $Fe_3O_4$ (not shown) and we find a negligible difference in the $H_2$ and $O_2$ yields between similarly prepared samples, which is contrary to thermodynamic equilibrium calculations that predict larger yields for cobalt ferrite compared to magnetite.[1] This further supports the conclusion that kinetics rather than thermodynamics limit our observed reaction rates.

Comparison of the amount of $H_2$ and $O_2$ produced by a net thermochemical cycle reveals an unexpected behaviour. At WS temperatures below 1200 °C, the amounts of $H_2$ and $O_2$ produced in our experiments correspond to those expected for a net stoichiometric reaction every cycle. This is clearly evident in Fig. 3 by the data scattered about the 1 : 2 trend line between 0 and 1000 μmol $g^{-1}$ $H_2$. However, above this temperature, a larger amount of $H_2$ is produced relative to $O_2$, with the data

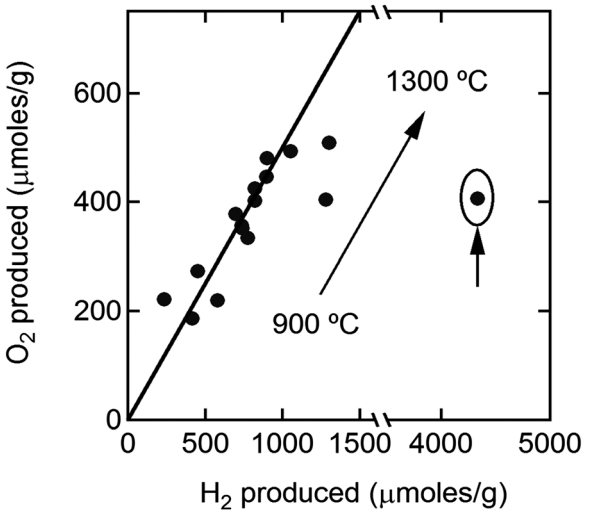


**Fig. 3** Total $O_2$ and $H_2$ evolved during each experiment for all conditions. Solid line represents the ideal stoichiometric ratio of $O_2$ : $H_2$ equal to 1 : 2. Circled data point indicates more $H_2$ produced than can be accounted for by simple stoichiometry (see text). The total amount of $O_2$ and $H_2$ are normalized to the mass of ferrite in the sample.

consistently falling below the ideal trend line. Interestingly, the $H_2$ plateau shown in Fig. 1 at 1100 °C becomes more pronounced at higher WS temperatures and does not decrease or return to baseline after several hours of water vapour exposure. We conjectured that this steady-state $H_2$ production is due to a catalytic process that becomes active at high temperatures.

To test this hypothesis, we performed an extended oxidation experiment for 6000 s and varied the temperature between 1250 °C and 1400 °C. The results are shown in Fig. 4. WS chemistry was initiated at 1300 °C and 30 vol% $H_2O$, and then the furnace temperature changed and the effect on the magnitude of the $H_2$ plateau monitored as a function of time. The results of these experiments are fully consistent with this hypothesis. At the outset of the experiment, the rapid initial rate of $H_2$ production and subsequent decay are indicative of the stoichiometric process in which O atoms liberated by WS are incorporated into the solid. After 1000 s, the $H_2$ production rate stabilizes at approximately 0.5 μmol $s^{-1}$ g. After holding the reactor at 1300 °C for 2000 s, the temperature was increased first to 1350 °C, then 1400 °C, while maintaining the flow of water vapour. In all cases, an increase in the furnace temperature produces a corresponding increase in the $H_2$ production rate, indicating the presence of an activated process that is able to continuously split water despite the net oxidation state of iron in the solid. We also observed continuous production of $O_2$ at each temperature, the amount of which was proportional to the thermally induced shifts in the $H_2$ plateau.

The $H_2$ plateaus observed at high temperature and long reaction times cannot be due to the slow oxidation of the sample, because the amount of $H_2$ generated is always much greater than the amount of $O_2$ liberated during the subsequent TR step (4332 μmol $H_2$ per g *vs.* 407 μmol $O_2$ per g, see circled data point in Fig. 3). In fact, more $H_2$ can be produced than that predicted if all of the available $Fe^{3+}$ in the sample were reduced to $Fe^{2+}$ and then re-oxidized. We can also rule out gas-phase water thermolysis and catalytic activity on extraneous surfaces in the SFR. Experiments performed without samples show no evidence of $H_2$ production until the temperature exceeds 1400 °C, and in that case, the amounts observed are insignificant compared to the magnitude of the $H_2$ plateaus measured in the presence of a sample.

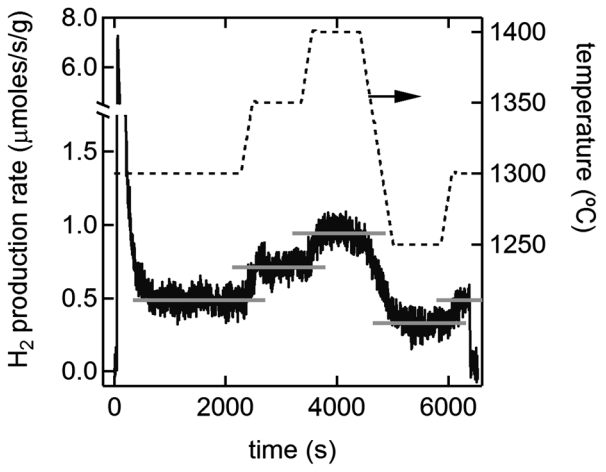


**Fig. 4** $H_2$ production rate measured during elevated oxidation temperatures (1250–1400 °C and 30 vol% $H_2O$) and prolonged exposure to water vapour. The $H_2$ production rate is normalized to the mass of ferrite in the sample.

The high-temperature steady-state $H_2$ production behaviour is indicative of a reaction operating at equilibrium, where both TR and WS occur simultaneously, analogous to that observed in water–gas shift (WGS) catalysis.[23] In the latter case, an oxidant ($H_2O$) and reductant (CO) react simultaneously with a metal oxide surface to produce $H_2$ and $CO_2$, whose yields are dictated by equilibrium. This is conceptually similar to the behaviour observed here, but reduction is achieved *via* a competition between TR and chemical reduction. These results indicate that it is possible to split $H_2O$, in the presence of the resultant solid solution formed by decomposition of $Co_{0.9}Fe_{2.1}O_4$, into $H_2$ and $O_2$ for an indefinite period of time without going to the extreme temperatures required for water thermolysis.[24] However, while scientifically interesting, a process such as this for solar $H_2$ production is likely not feasible because $H_2$ and $O_2$ must be separated before they recombine. We are able to observe coevolution of $H_2$ and $O_2$ in this experiment because they are highly dilute and the extremely short gas residence time (of order ms) in the SFR effectively quenches recombination. These features of our experiment likely explain why this has not been reported by researchers using traditional reactor configurations. In addition, the temperature required to efficiently operate this non-stoichiometric process is in excess of 1400 °C, which further complicates production-scale reactor designs. In light of this behaviour, we have chosen to limit our kinetic analysis to temperatures below 1100 °C where the stoichiometric WS reaction dominates. It is important to note that other research groups reporting kinetics on similar iron-containing composites should also consider the high-temperature catalytic process when interpreting their results.

### Numerical analysis of water oxidation kinetics

The intent of the numerical analysis is to separate experimental artefacts, such as detector time lag and gas-phase dispersion, from the observed time-dependent $H_2$ production rate signal to obtain accurate values of the material-specific kinetic rates. This will enable us to identify rate-controlling mechanisms and their associated kinetic parameters, within the context of solid-state kinetic theory, using the complete dataset we obtained over its entire time domain. Thus, our model-based approach is markedly different from kinetic investigations of similar reactions reported in the literature.[3,15,16]

Our numerical approach tested 14 individual mechanisms that span four distinct families of solid-state reaction phenomena, including nucleation and growth, geometrical contraction (shrinking core), diffusion, and reaction-order behaviours. In performing the fits, it rapidly became clear that no single mechanism could fit the $H_2$ production rate across the entire time interval of the experiment. In particular, F2 (second-order reaction, analogous to homogenous kinetics) and D1 (1-D diffusion), which are physically reasonable mechanisms in the context of our materials, yield much better fits when combined

 

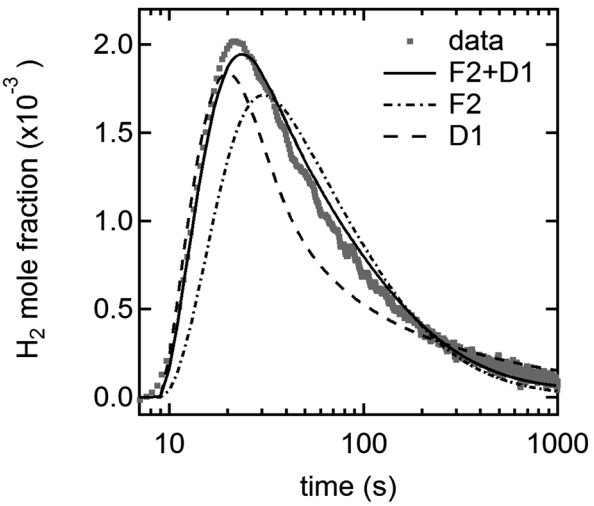


**Fig. 5** $H_2$ mole fraction as a function of time (solid points) measured at 1100 °C and 40 vol% $H_2O$ compared to simulations (solid and dashed lines) derived from solid-state kinetic models. The solid line combines F2 and D1 functionals, the dashed lines are simulations using either F2 or D1 as labelled (see text).

than when either is used individually. As seen in Fig. 5 (note the logarithmic scale on the *x*-axis), the early phase of the reaction (the first 20 seconds) is described well by D1, but this mechanism under-predicts $H_2$ production at longer times between 20 and 300 s. Similarly, the F2 mechanism fails to capture the initial peak correctly and tends to over-predict $H_2$ production rates past the peak. The same is true for all mechanism pairs that were evaluated numerically, none of which yields a lowered-value least-squares objective than the F2 + D1 pair (see Fig. S5 and Table S1 in the ESI†).

The high quality of the dual-mechanism (F2 + D1) fit to the experimental data is maintained over the entire range of WS conditions we examined. Shown in Fig. 6 is a typical example where the mole fraction of hydrogen is plotted as a function of time for WS at three temperatures between 900 and 1100 °C and 30 vol% $H_2O$. The model fit was generated from a least squares optimization over the entire dataset comprised of 12 experimental $H_2$ production rate curves (measured at 1.8 Hz for 1000 s), taken at three different water vapour volume fractions (20, 30, and 40 vol%), and three different temperatures (900, 1000, and 1100 °C). The RSSQ in eqn (7) was calculated at every time step, meaning that greater than 20 000 data points were considered during each iteration of the optimizer. As seen here the WS activity at each of these temperatures, as well as for the remaining nine reactor conditions (not shown for clarity), is well represented by the combined F2 and D1 kinetic models.

A comparison of the RSSQ values for other mechanism pairs provides further confirmation that (F2 + D1) describes the kinetic data considerably better than any of the other dual-mechanism possibilities considered. The top panel of Fig. 7 shows the minimum RSSQ value obtained for a subset of the model pairs we tested, with the magnitude indicated by the diameter of the symbol located at the intersection between grid lines. Only F2 and D1 are labelled in this graph for clarity; however, this mechanism subset includes three order-based models and three diffusion-based models, for a total of nine model pairs. The smallest symbol is located at the intersection between F2 and D1 grid lines. The relatively large symbol sizes of nearest neighbours indicate that the (F2 + D1) pair is a strong attractor, giving confidence that the fitting procedure found the global minimum in the response surface and the result is

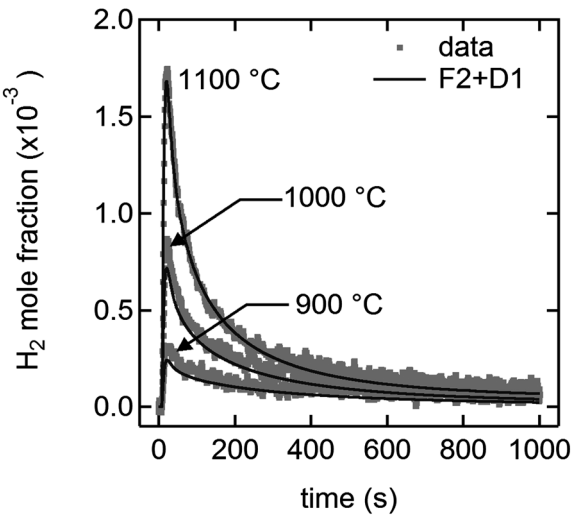


**Fig. 6** $H_2$ mole fractions as a function of time (solid points) compared to simulations (solid lines) derived from a solid-state model that combines F2 and D1 functionals for three WS temperatures at 30 vol% $H_2O$.

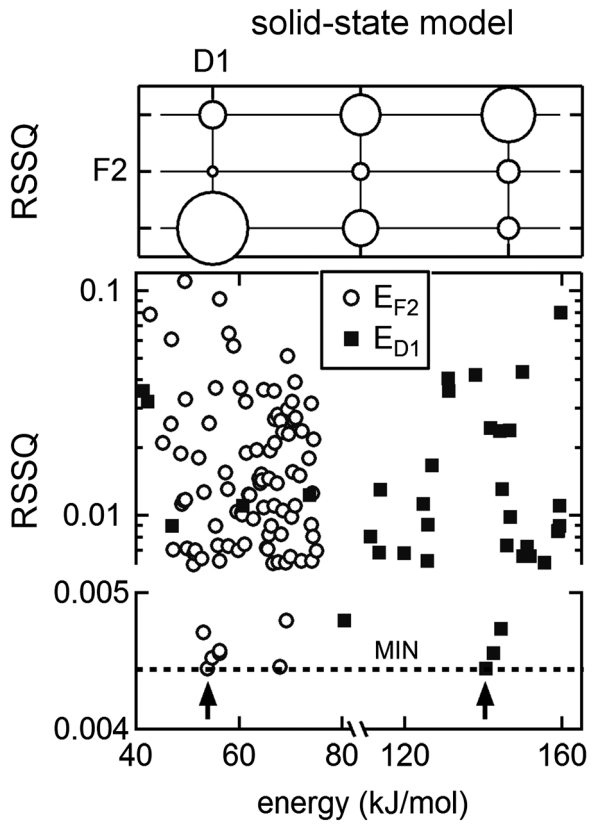


**Fig. 7** Values of RSSQ (see eqn (7)) for solid-state model pairs (top panel), and the apparent activation energy for F2 and D1 (bottom panel).

unique. The bottom panel in Fig. 7 plots the RSSQ values for the two kinetic parameters ($E_{F2}$ and $E_{D1}$) obtained while the fitting routine iteratively sampled the constrained region around these two constants. Here again, there is a well-defined minimum in the response surface (marked by black arrows in Fig. 7), indicating a unique solution was obtained from the Differential Evolution algorithm. The apparent activation energies corresponding to this minimum RSSQ are 53.9 kJ mol$^{-1}$ for the second-order reaction process (F2) and 141 kJ mol$^{-1}$ for the diffusion process (D1). The significance of these values with respect to the reaction mechanism is discussed below.

The end result of finding a model that fits the experimental data is not limited to the kinetic parameters obtained, or the ability to simulate $H_2$ production in the SFR. Valuable mechanistic insight can be obtained by determining the relative importance of one kinetic process over the other during the course of the oxidation. We computed this from the first derivative of the extent of reaction variable ($\alpha_i$) for F2 and D1 as a function of time, which is plotted in Fig. 8. The sum of these two derivatives is proportional to the rate of $H_2$ production (eqn (6)) at 1100 °C and 40 vol% $H_2O$. In the first 11 s, it appears that oxidation of the iron located on the active areas of the embedded cobalto-wustite particles reacts first, accounting for 69% of the hydrogen produced during this time interval. At later times, however, the D1 reaction shuts down, limiting the amount of hydrogen generated by this pathway to 36% of the total (288 μmol g$^{-1}$ out of a total 800 μmol g$^{-1}$ $H_2$). In contrast, the rate of F2 decreases steadily during the entire experiment, but overall is responsible for the remaining 64% of the hydrogen produced (512 μmol g$^{-1}$ $H_2$).

### Mechanism of water oxidation

The kinetic analysis just described suggests a process in which two different sources of reduced iron contribute to the production of $H_2$. The diagram in Fig. 9 and reactions (8) through (11) (written in Kröger–Vink notation) outline the proposed solid-state chemistry.

$$2Fe''_{Zr} \rightarrow 2Fe'_{Zr} + 2e' \quad (8)$$

$$H_2O(g) + V_O^{\cdot\cdot} + 2e' \rightarrow H_2(g) + O_O^{\times} \quad (9)$$

$$H_2O(g) + V_O^{\cdot\cdot} + 2Fe''_{Zr} \rightarrow H_2(g) + O_O^{\times} + 2Fe'_{Zr} \quad (10)$$

$$3Fe'_{Me} + \frac{4}{3}O_O^{\times} \rightarrow \frac{4}{3}V_O^{\cdot\cdot} + \frac{8}{3}e' + V_{Me}''' + 2Fe_{Me}^{\times} + \frac{1}{3}Fe_3O_4 \quad (11)$$

Reaction (8) represents the oxidation of the reduced iron dissolved in the $ZrO_2$ lattice. Reaction (9) describes water reacting at the external interface of the composite converting oxygen vacancies to lattice oxygen. Summing reactions (8) and (9) gives reaction (10), which is the net result of iron oxidation and incorporation of lattice oxygen into the support phase and is governed by a second-order power law relation (F2). The oxidation of cobalto-wustite at the internal interface (labelled "b" in Fig. 9) is captured by reaction (11). The defect chemistry denoted in reaction (11) was derived in accordance with the assumptions adopted for oxidation of similar ferrite-based spinels.[25,26] Here cation, defect, and coordination distributions are ignored; hence Me represents all cations in the system and it is assumed that the concentration of $Co^{3+}$ is insignificant so that the defect chemistry describes valence state changes in the Fe exclusively. The precise mechanism of charge compensation during this process is unclear, but our results indicate that this reaction rate is limited by diffusion (D1). We assume that the ionic defect $Fe'_{Me}$ is transported through the growing ferrite layer, which is consistent with the accepted mechanism of wustite oxidation at high-temperature. Therefore, according to the schematic in Fig. 9, oxygen vacancies are consumed at the outer surface by reaction with steam, generating hydrogen, and are produced at the interface between the zirconia support and embedded iron oxide particle. The incorporation of lattice oxygen into the support is described by reaction (10), and reactions (10) and (11) occur in parallel.

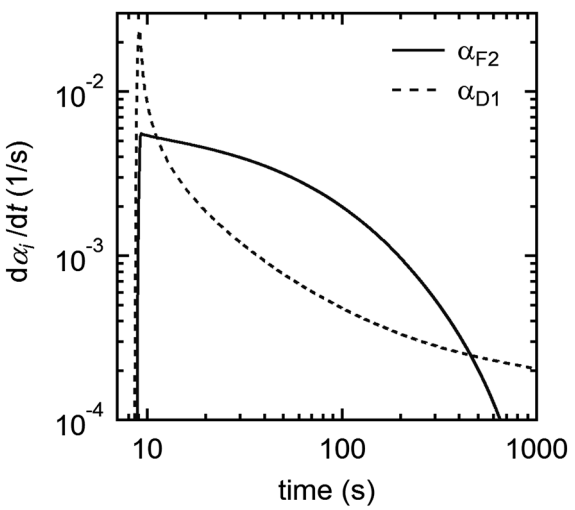


**Fig. 8** The first derivative of the extent of reaction variable ($\alpha_i$) for F2 and D1 models resulting from the simulation of a $H_2$ production rate curve at 1100 °C and 40 vol% $H_2O$.

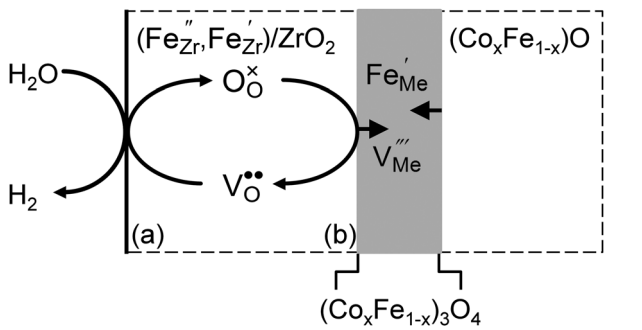


**Fig. 9** Schematic illustrating the oxidation of $Fe^{2+}$ located in the $ZrO_2$ lattice and in the embedded iron oxide particle, initiated by reaction with $H_2O$. The dark solid line at left is the external gas–solid interface (a), the grey bar is the advancing spinel phase growing from the embedded cobalto-wustite particle, and (b) marks the internal interface between support and particle through which iron must diffuse in order to react with lattice oxygen from the $ZrO_2$.

 

Qualitatively, an initial rapid reaction occurs between the $(Co_xFe_{1-x})O$ solid solution and lattice oxygen at the highly reactive areas of the embedded cobalto-wustite particles seen in Fig. 2(f). However, the ferrite product layer $(Co_xFe_{1-x})_3O_4$ that quickly forms has a low ion permeability, causing the rate of this process to rapidly decay (the D1 curve falls below F2 in Fig. 8). We note that the ferrite layer at this internal interface does not form instantaneously and in all likelihood the nucleation of this layer would not be well described by D1. Neglecting this short-lived process impacts the initial slope of the simulated production curve and slightly underpredicts the amount of $H_2$ attributed to the D1 mechanism. No attempt was made to resolve this behaviour over the rising edge of the water vapour input pulse. The slower, but more continuous reaction described by F2 simultaneously produces $H_2$ at a rate that decays as the $Fe''_{Zr}$ impurity is depleted. As will be shown below, these observations are consistent with both the results of our experiments and related investigations by others that describe the high-temperature phases and species transport in iron oxides and zirconia.

With two distinct forms of reduced iron present, we expect that transport and reaction between them cannot be described by a single rate-governing process. The SEM images in Fig. 2 show the zirconia substrate and cobalt ferrite phases segregate during high-temperature heat treatment. In addition, it is well known that both $Fe^{2+}$ and $Fe^{3+}$ are soluble in both $ZrO_2$[27,28] and YSZ.[29] Experiments by Kodama *et al.* for $ZrO_2$ and YSZ suggest that this dissolved iron is more reactive than the iron contained in the cobalto-wustite phase that forms when cobalt ferrite is reduced.[17] We hypothesize that this apparent difference in reactivity is actually the result of the formation of a diffusion barrier at the cobalto-wustite/ferrite interface that forms during WS, which effectively isolates the cobalto-wustite phase from oxygen permeating through the $ZrO_2$ lattice. Oxygen ion accessibility to the dissolved iron impurity in the zirconia lattice is not likewise encumbered.

A recent investigation of $CO_2$ splitting by Coker *et al.* using $Fe_3O_4$ supported on YSZ provides strong evidence that this hypothesis is correct.[30] These authors mapped the exchange of $^{16}O$ with $^{18}O$ oxygen in a ferrite/YSZ composite monolith using isotopically labelled $CO_2$ as the reactant. They find that a substantial amount of the CO generated during oxidation of reduced ferrite can be attributed to the iron dissolved in the YSZ lattice, rather than the grains of a separate iron oxide phase embedded within the YSZ matrix. Using TOF-SIMS they found that oxygen from $C(^{18}O)_2$ permeates the YSZ matrix several orders of magnitude faster at 1100 °C than the thermochemical re-oxidation of the reduced iron species by $CO_2$ at the same temperature. In addition, oxygen permeation into bulk iron oxide particles embedded in the YSZ matrix is limited to the outer surface of the particle, even after a 7 h exposure to $C(^{18}O)_2$ at 1100 °C. For iron oxide particles with characteristic dimensions of a few microns or less, a 7 h exposure was sufficient to re-oxidize a majority of the reduced material; however, the interior of particles larger than this remained unreacted at these conditions. As a result, material formulations with iron loadings greater than the iron solid solubility limit in YSZ (~9 mass %)[30] exhibit significantly lower iron utilization on a mass basis, as well as slower oxidation kinetics, because the excess iron segregates to form large particles that cannot fully participate in the re-oxidation reaction.

Together, these observations (fast oxygen anion transport/exchange through YSZ; oxygen permeation into the embedded bulk iron oxide particles limited to the outer surface; and under-utilization of iron in samples where the mass loading exceeds the zirconia solid solubility limit) indicate that the kinetics of iron oxidation in our $ZrO_2$ composite can be described by the aforementioned solid-state processes occurring in parallel. At this point it is unclear whether F2, which accounts for the reaction of the dissolved iron, represents a surface-mediated process that governs the dissociation of water molecules, or the oxidation of $Fe''_{Zr}$ defect in the $ZrO_2$ lattice. Both of these rate-limiting processes are described by second-order reaction kinetics. Rate expressions and kinetic parameters for the complete oxidation model are listed in Table S2.†

## Discussion and conclusions

The experimental method and model-based analytical approach employed here to resolve the kinetic behaviour of similar two-step thermochemical redox material systems are markedly different from other work in the literature. Most notably, our method resolves and makes use of the entire time domain, including reaction initiation, rather than using a simple peak-rate analysis or universal "Master Plot" analysis,[20] and addresses the fact that multiple reaction mechanisms are operative simultaneously. This allows temporal artefacts associated with instrument response and experimental protocols to be separated from the actual $H_2$ production kinetics, so that multiple solid-state mechanisms acting simultaneously can be considered. Previous investigations employed either single-step mechanisms or sequential processes to account for the time dependence of the gas splitting rate. Moreover, these studies considered only the kinetics of bulk ferrites in their analysis, while in practice redox-active phases are often mixed with solid supports to prevent undesirable sintering.[2–4,12,17,30] Other than the investigation by Coker *et al.* discussed above,[30] the effects of the support on iron oxide water splitting kinetics have not been addressed and kinetic treatments reported to date do not account for the possibility of multiple physical and/or chemical phenomena occurring simultaneously.

In our analysis, the kinetic model D1 represents a classic parabolic rate law for one-dimensional diffusion (see Table 1). This is reasonable, since one-dimensional behaviour is expected for transport across a thin oxide layer when the layer thickness is much smaller than the particle diameter. Such behaviour was found by Coker *et al.*, who observed using TOF-SIMS that $^{18}O$ from isotopically labeled $CO_2$ was concentrated at the surface of iron oxide particles embedded in YSZ.[30] Considering that our oxidation times were on the order of 1000 s *vs.* 7 hours at temperatures comparable to those used by Coker *et al.*, we expect that our material system will also behave in a one-dimensional fashion.

In cases where the D1 rate law is applicable to iron oxidation to form magnetite ($Fe_3O_4$), it is generally accepted that the rate-limiting process is the outward diffusion of iron through the product layer.[31] Dieckmann *et al.*[32] and Lu *et al.*[33] performed cation tracer experiments with $^{59}Fe$ and $^{60}Co$ on both stoichiometric and non-stoichiometric spinels and identified two mechanisms by which diffusion can occur between 900 and 1400 °C: a vacancy mechanism that is operative at high oxygen activities having a negative activation energy ($E_a$) of $-140$ kJ mol$^{-1}$, and movement of bulk interstitial iron cations at low oxygen activities with an $E_a$ of 615 kJ mol$^{-1}$. The activation energy for D1 of 141 kJ mol$^{-1}$ extracted from our analysis is not in good agreement with either value. Interestingly, activation energies reported in the literature for oxidation of Fe[34] and FeO[15,16] at lower temperatures are in the range of 100–160 kJ mol$^{-1}$, and those measured by the aforementioned researchers under redox conditions similar to ours are also in agreement.

Since the oxygen activity was not controlled in either our experiments or in these previous reports, it is not possible to say conclusively what elementary mechanism (*i.e.*, interstitial or vacancy) controls the rate of the diffusion process, nor is it necessary. It is clear from the work of Dieckmann *et al.* and Lu *et al.* that the diffusion coefficients are highly dependent upon the temperature, the oxygen activity, and the oxide stoichiometry (*i.e.*, cobalt content). While the value of $E_a$ (141 kJ mol$^{-1}$) we obtain suggests that neither the vacancy nor interstitial mechanisms alone control the rate, it is possible that our parameterized D1 model is reflective of a transitional state between these two elementary processes. This may be attributed to: (1) the equilibrium gas-phase oxygen activity changes by three orders of magnitude under our experimental conditions during the course of the oxidation and (2) the high sensitivity of the vacancy and interstitial diffusion constants to both oxygen activity and cobalt content in the spinel. For the latter, the diffusion constants for metal vacancies decrease by several orders of magnitude, while that for the interstitials increase, as the spinel composition approaches $CoFe_2O_4$. Both of these effects have a large impact on the concentration of defects that govern cation diffusion,[33] and thus the rate controlling mechanism. Unfortunately more definitive conclusions cannot be made without a far more extensive experimental program than was possible here.

The order-based reaction F2 is also activated, with an energy obtained from the fit ($E_a$) = 53.9 kJ mol$^{-1}$ and a reaction order for the water mole fraction ($\gamma$) = 1.22 (see Table S2†). The kinetic expression presented in eqn (3) and Table S2† represents a global reaction, which takes an Arrhenius form and describes either surface-mediated processes involving the adsorption and dissociation of $H_2O$ molecules, followed by surface exchange of O atoms through vacancies and $H_2$ desorption, *or* chemical reactions internal to the solid solution. We cannot confirm which of these possibilities is rate limiting, but the aforementioned order-based model yields a better fit to the experimental observation than other solid-state mechanisms involving diffusion and/or nucleation and growth, even when paired with D1 (see Fig. S5 and Table S1†).

If a chemical reaction is the rate-limiting step, then presumably oxygen transport through the ferrite/$ZrO_2$ composite must be faster by comparison. Activation energies for oxygen diffusion in both monoclinic and cation-stabilized cubic zirconia have been reported. For undoped monoclinic $ZrO_2$, their magnitude is dependent on the diffusion mechanism (volume *vs.* interface), but are in any case $\geq$ 190 kJ mol$^{-1}$.[35] It is also well known that doping with various metal cations dramatically increases the ionic conductivity. For example, yttria doping reduces $E_a$ for oxygen diffusion to as little as 75 kJ mol$^{-1}$.[36] This value is still greater than what we obtain by fitting the F2 mechanism. Furthermore, a diffusion mechanism does not adequately describe the $H_2$ production rate behaviour. One possible explanation is that treating zirconia with hydrogen creates surface oxygen vacancies, for which $E_a$ is only 20 kJ mol$^{-1}$ when measured over previously reduced $ZrO_2$.[37] In addition, the number of surface vacancies formed is influenced by the relative amounts of $H_2O$ and $H_2$ in the feed stream, the flow rate, and iron impurities in the $ZrO_2$, which are all circumstances that pertain to the conditions of our experiments as well as to previously reported rates. Here again, the parameterized F2 model is reflective of a complex reaction network that exhibits energetics which cannot be attributed to a single elementary process.

In summary, the quantitative data and insights into ferrite reactivity gained from this investigation fill a critical gap in the knowledge base required to develop high-fidelity computational models for designing solar receiver reactors. Maximizing the solar-to-hydrogen conversion efficiency requires system designs in which the reaction chemistry within the oxidation and reduction zones is matched to the corresponding material transport rates, and thus the transit times, for each zone. Clearly, optimization of material properties and reactor design is an iterative process, and for complex composite materials such as cobalt ferrite/$ZrO_2$, validated models based on experimental rate constants will be an invaluable enabling resource for rational process design.

## Acknowledgements

This work was supported by the National Science Foundation *via* Grant CBET 0966201, by the U.S. Department of Energy Fuel Cell Technologies Program *via* the Solar Thermochemical Hydrogen (STCH) directive, and by Laboratory Directed Research and Development at Sandia National Laboratories. Sandia is a multiprogram laboratory operated by Sandia Corporation, a Lockheed Martin Company, for the United States Department of Energy's National Nuclear Security Administration under Contract DE-AC04-94AL85000.

## Notes and references

1 M. D. Allendorf, *Energy Fuels*, 2008, **22**, 4115–4124.
2 T. Kodama, N. Gokon and R. Yamamoto, *Sol. Energy*, 2008, **82**, 73–79.
3 M. Neises, M. Roeb, M. Schmücker, C. Sattler and R. Pitz-Paal, *Int. J. Energy Res.*, 2010, **34**, 651–661.
4 T. Kodama, Y. Kondoh, R. Yamamoto, H. Andou and N. Satou, *Sol. Energy*, 2005, **78**, 623–631.

 

5 T. Kodama, *Prog. Energy Combust. Sci.*, 2003, **29**, 567–597.
6 R. B. Diver, J. E. Miller, M. D. Allendorf, N. P. Siegel and R. E. Hogan, *J. Sol. Energy Eng.*, 2008, **130**, 041001.
7 N. Gokon, S. Takahashi, H. Yamamoto and T. Kodama, *J. Sol. Energy Eng.*, 2009, **131**, 011007.
8 H. Kaneko, T. Miura, A. Fuse, H. Ishihara, S. Taku, H. Fukuzumi, Y. Naganuma and Y. Tamaura, *Energy Fuels*, 2007, **21**, 2287–2293.
9 M. Roeb, M. Neises, J.-P. Säck, P. Rietbrock, N. Monnerie, J. Dersch, M. Schmitz and C. Sattler, *Int. J. Hydrogen Energy*, 2009, **34**, 4537–4545.
10 C. Agrafiotis, M. Roeb, A. G. Konstandopoulos, L. Nalbandian, V. T. Zaspalis, C. Sattler, P. Stobbe and A. M. Steele, *Sol. Energy*, 2005, **79**, 409–421.
11 S. Lorentzou, C. C. Agrafiotis and A. G. Konstandopoulos, *Granular Matter*, 2008, **10**, 113–122.
12 J. E. Miller, M. D. Allendorf, R. B. Diver, L. R. Evans, N. P. Siegel and J. N. Stuecker, *J. Mater. Sci.*, 2008, **43**, 4714–4728.
13 P. Charvin, S. Abanades, G. Flamant and F. Lemort, *Energy*, 2007, **32**, 1124–1133.
14 M. H. Khedr, A. A. Omar and S. A. Abdel-Moaty, *Mater. Sci. Eng., A*, 2006, **432**, 26–33.
15 K. S. Go, S. R. Son and S. D. Kim, *Int. J. Hydrogen Energy*, 2008, **33**, 5986–5995.
16 P. G. Loutzenhiser, M. E. Galvez, I. Hischier, A. Stamatiou, A. Frei and A. Steinfeld, *Energy Fuels*, 2009, **23**, 2832–2839.
17 T. Kodama, Y. Nakamuro and T. Mizuno, *J. Sol. Energy Eng.*, 2006, **128**, 3–7.
18 J. R. Scheffe, M. D. Allendorf, E. N. Coker, B. W. Jacobs, A. H. McDaniel and A. W. Weimer, *Chem. Mater.*, 2011, **23**, 2030–2038.
19 W. C. Chueh and S. M. Haile, *ChemSusChem*, 2009, **2**, 735–739.
20 F. J. Gotor, J. M. Criado, J. Malek and N. Koga, *J. Phys. Chem. A*, 2000, **104**, 10777–10782.
21 J. Šesták and J. Málek, *Solid State Ionics*, 1993, **63–65**, 245–254.
22 I. Wolfram Research, *Mathematica Edition: Version 8.0*, Wolfram Research, Inc., 2010.
23 P. C. Ford, *Acc. Chem. Res.*, 1981, **14**, 31–37.
24 C. Etievant, *Sol. Energy Mater.*, 1991, **24**, 413–440.
25 S. Aggarwal and R. Dieckmann, *Phys. Chem. Miner.*, 2002, **29**, 695–706.
26 F.-H. Lu and R. Dieckmann, *Solid State Ionics*, 1992, **53-56**, 290–302.
27 S. Figueroa, J. Desimoni, P. C. Rivas, M. C. Caracoche and O. de Sanctis, *J. Am. Ceram. Soc.*, 2006, **89**, 3759–3764.
28 J. D. Ferguson, A. W. Weimer and S. M. George, *J. Vac. Sci. Technol., A*, 2005, **23**, 118–125.
29 F. L. Garcia, V. G. de Resende, E. De Grave, A. Peigney, A. Barnabe and C. Laurent, *Mater. Res. Bull.*, 2009, **44**, 1301–1311.
30 E. N. Coker, J. A. Ohlhausen, A. Ambrosini and J. E. Miller, *J. Mater. Chem.*, 2012.
31 A. Atkinson, M. L. O'Dwyer and R. I. Taylor, *J. Mater. Sci.*, 1983, **18**, 2371–2379.
32 R. Dieckmann, M. R. Hilton and T. O. Mason, *Ber. Bunsenges. Phys. Chem.*, 1987, **91**, 59–66.
33 F.-H. Lu, S. Tinkler and R. Diekmann, *Solid State Ionics*, 1993, **62**, 39–52.
34 R. Y. Chen and W. Y. D. Yuen, *Oxid. Met.*, 2003, **59**, 433–468.
35 U. Brossmann, R. Wurschum, U. Sodervall and H. E. Schaefer, *J. Appl. Phys.*, 1999, **85**, 7646–7654.
36 M. Kilo, C. Argirusis, G. Borchardt and R. A. Jackson, *Phys. Chem. Chem. Phys.*, 2003, **5**, 2219–2224.
37 D. Eder and R. Kramer, *Phys. Chem. Chem. Phys.*, 2002, **4**, 795–801.